

RESEARCH

Open Access



Spatial localization of hotspots in Fano-resonant plasmonic oligomers for surface-enhanced coherent anti-Stokes Raman scattering

Arpan Dutta^{1*} and Erik M. Vartiainen²

Abstract

Realization of Fano resonance in plasmonic oligomers is often exploited to design efficient plasmonic substrates for surface-enhanced coherent anti-Stokes Raman scattering. Disk-type Fano-resonant plasmonic oligomers are widely used to enhance the Raman signal of the probe material. Generally, hot spots are generated in those oligomers at different spatial locations at different wavelengths and only a few spatially overlapping hot spots at multiple wavelengths can be achieved with oblique incidence of excitation light. In this work, we proposed hexagonal gold nanoparticle based Fano-resonant plasmonic oligomers that can yield higher number of spatially overlapped hot spots compared to the disk type oligomers even with the normal incidence of excitation light. The oligomers were numerically modelled and optimized for surface-enhanced coherent anti-Stokes Raman scattering with 780 nm pumping and 500–1800 cm^{-1} Raman signature region. The Fano lineshape was engineered to ensure near-field energy coupling at pump while enhancing the coherent anti-Stokes Raman signal at the far field. Our computational studies explored the purely electric origin of Fano resonance in those oligomers and provided maximum Raman enhancements of 10^{12} – 10^{13} from them to enable single-molecular level applications. Our findings provide a way to realize fabrication-friendly nanostructures with higher number of spatially localized hotspots for improving the Raman detection sensitivity.

Keywords: Fano resonance, Plasmonic oligomers, Coherent anti-Stokes Raman scattering

Introduction

The ability of Raman spectroscopy (RS) to provide accurate chemical ‘fingerprint’ of probed material [1–3] enables its utilization as a powerful analytical tool in different scientific and industrial fields [4, 5]. Development of integrated optical technologies and ultrafast lasers made RS a unique diagnostic tool for non-destructive [6] and non-invasive analysis [7]. In spite of all acclaimed potentials of RS, its real-life implementations are often become challenging due to the inherited weakness of the

Raman response of the probe [8]. A linear approach to overcome the aforementioned limitation of RS is surface-enhanced Raman spectroscopy (SERS) where a plasmonic substrate is used to amplify the Raman signal of the probe material [8–12]. Biosensing at nanoscale [13–15] and single molecule detection [16–19] become realizable nowadays with the suitable application of SERS. Another approach of strengthening the Raman signal is coherent anti-Stokes Raman scattering (CARS) where the Raman response is amplified with the help of a nonlinear optical four-wave mixing (FWM) process, instead of a plasmonic substrate [20–27]. In CARS, two laser beams, the so-called pump (ω_p) and Stokes (ω_s), are focused into a sample and its molecular vibration

* Correspondence: arpan.a.dutta@jyu.fi

¹Department of Physics and Nanoscience Center, University of Jyväskylä, Jyväskylä, Finland

Full list of author information is available at the end of the article

modes are driven by the beat frequencies ($\omega_p - \omega_s$) of the laser beams and simultaneously probed by a third (probe, ω_{prb}) laser beam to produce an output signal at the blue-shifted anti-Stokes frequency ($\omega_p - \omega_s + \omega_{prb}$). In CARS micro-spectroscopy, the pump and probe beams are obtained from the same narrow-band pulsed laser and the Stokes from a broadband (femtosecond or supercontinuum) laser source [21–27]. CARS signal can further be enhanced by employing a plasmonic substrate along with the existing nonlinear process [12, 28–30]. Surface-enhanced CARS (SECARS) is such a method in which the Raman signal enhancement can attain a much higher level compared to the normal RS, SERS, or CARS alone [29, 30]. Achievement of single-molecular level sensitivity in molecular sensing become possible with SECARS [28].

Designing plasmonic substrates for multi-frequency based spectroscopic techniques such as SECARS is demanding since the optical properties of the substrate has to be engineered such a way that its plasmon resonances would overlap with all intended spectral regimes of the spectroscopic technique. Realization of Fano-resonant plasmonic (or Fano-plasmonic) oligomers is one option [28, 30]. In a plasmonic oligomer, metal nanoparticles (NPs) are clustered with optimal sizes, shapes and inter-particle distances to obtain desired optical responses from the oligomer. Hybridization between the localized surface plasmon resonances (LSPR) of the NPs engendered Fano resonance (FR) in the scattering (or extinction) profile of the oligomer, manifested as two peaks having one dip between them in the corresponding scattering (or extinction) lineshape [31, 32]. The scattering peaks, called as the super-radiant (or bright) mode of FR, are generated due to the constructive interference between the LSPR modes of the NPs when the plasmon oscillations in all NPs are ‘in phase’. The scattering dip, which is also known as the sub-radiant (or dark) mode of FR, is a result of the destructive interference between the LSPR modes of the NPs when the plasmon oscillations in all NPs are not ‘in phase’ [33–36]. Tuning of FR at the desired spectral regions can be obtained by optimizing the size, shape, thickness or height, and material of the NPs present in the oligomer while optimization of the interparticle gap provides a way to control the degree of the hybridization between the LSPR modes of the NPs [32, 37]. Theoretical explanation behind the origin of FR in plasmonic oligomers can be found elsewhere [36, 38–43].

Implementation of Fano-plasmonic oligomers in SECARS requires spectral overlap of the sub-radiant mode of FR (i.e. the scattering dip or Fano dip) with the pump frequency. The two super-radiant modes of FR (i.e. the scattering peaks or Fano peaks), situated in the red and blue side of the Fano dip, has to be tuned with the Stokes and the

CARS frequencies, respectively [28, 30]. Such strategy ensures an enhancement of the output light i.e. the CARS signal at the far field along with an optimized coupling between the excitation energy and the plasmonic substrate at the pump wavelength [28]. The achievable Raman signal enhancement in SECARS depends on the electric field enhancements at the pump, Stokes, and CARS frequencies as well as the spatial localization of the hot spots (i.e. confined regions with highly localized electromagnetic energy) at the same position at those three frequencies [30]. In general, hot spots are distributed at different positions over the substrate geometry at different wavelengths and spatial overlap of them can be achieved with the oblique incidence of excitation (i.e. pump) light as reported earlier [30]. In addition, higher number of hot spots is favorable for the optimal intensification of SECARS signal and in disk-type Fano-plasmonic oligomers, only a few hot spots are possible to achieve as shown in previous works [28, 30]. Eventually, realizing plasmonic substrates that can provide higher number of spatially localized hotspots is most desirable for improving the sensitivity of SECARS.

In this article, two Fano-plasmonic oligomers, a quadrumer and a heptamer, consisting of hexagonal-shaped gold NPs, are proposed as SECARS substrates. The oligomers are numerically modelled and optimized using the finite element method (FEM) for CARS applications where the pump wavelength is 780 nm. The targeted Raman signature zone is considered as the favorable ‘fingerprint region’ of analytes, i.e. 500–1800 cm^{-1} [44]. For the aforementioned Raman signature regime, the Stokes wavelengths cover approximately 810–908 nm and the corresponding CARS window becomes 683–753 nm. Unlike the existing literature [28, 30, 33, 34, 40, 45–47], the hexagonal shape is chosen for the nanoparticles present in the oligomers since the hexagonal geometry offers a higher number of nanogaps than that in the disk-type geometry. Our computational studies reveal that the hexagonal NP based Fano-resonant oligomers can yield higher number of spatially localized hot spots compared to the disk-type oligomers even with the normal incidence of the excitation light. Our numerical analysis also explores the origin of FR in the proposed oligomers in terms of the complex phase relations between the induced dipole moments of the hexagonal NPs. Such findings are important in the context of designing plasmonic substrates for SECARS and for multi-photon based spectroscopic techniques in general since they could provide a way to reach high sensitivity in Raman detection with fabrication-friendly nanostructures.

Methods

The oligomers were numerically modelled and optimized for CARS applications using a commercial FEM package (COMSOL Multiphysics version 5.4). In the

simulation environment, a single oligomer was kept on top of a glass (SiO_2) substrate and air was considered as the surrounding medium. The whole simulation space was $2\ \mu\text{m} \times 2\ \mu\text{m} \times 2\ \mu\text{m}$ and perfectly matched layers (PMLs) were used at all the boundaries of it to prevent spurious reflections. The near- and far-field (optical) properties of the oligomers were calculated for the normal incidence of light with electric field along the oligomer's main axis (as illustrated in Fig. 1) using the scattered-field formulation (wave optics module) of COMSOL [48]. The complex dielectric function of gold was collected from the experimental data reported by Johnson and Christy [49]. The nondispersive refractive indices of air and SiO_2 were taken as 1.00 and 1.45, respectively.

Results and discussion

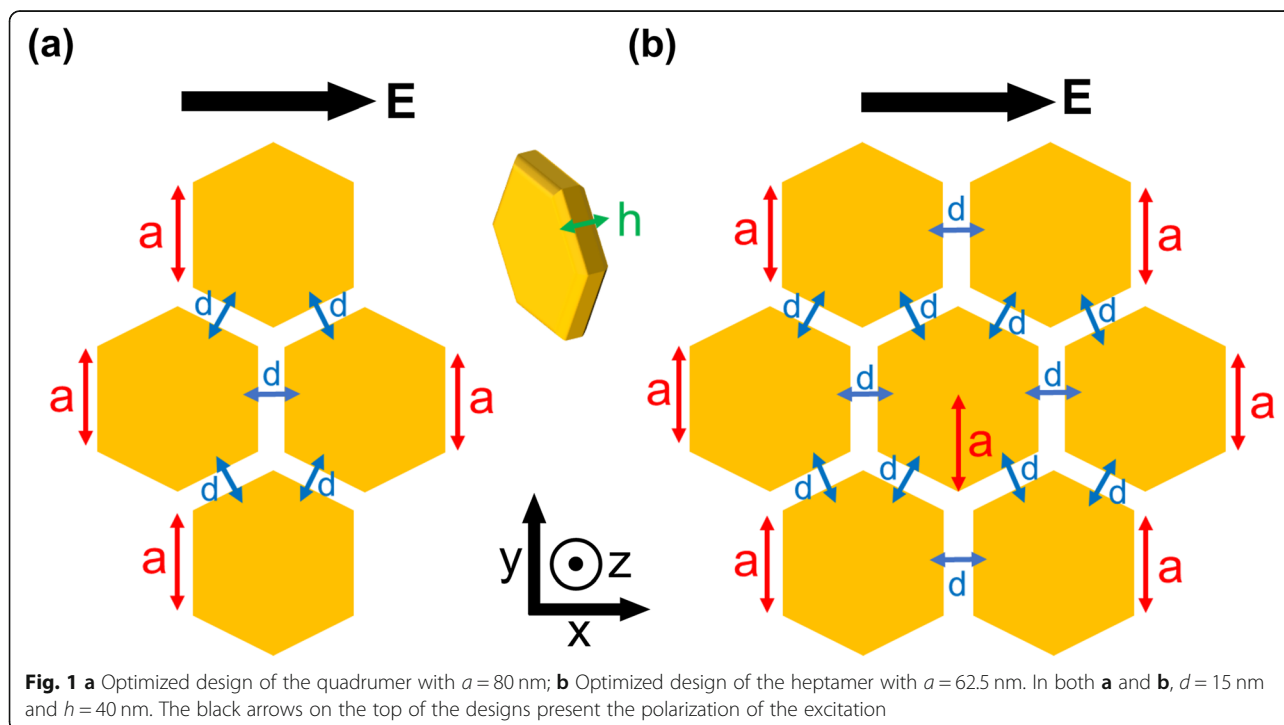
The oligomers were modelled and optimized using FEM so that their FR would spectrally overlap with the intended pump, Stokes and CARS regions. The schematic designs of the quadramer and the heptamer are presented in Fig. 1. The quadramer, depicted in Fig. 1a, contains four identical hexagonal NPs having same sizes (hexagon side length a) as well as equal thicknesses (h) and interparticle gaps (d). The heptamer, illustrated in Fig. 1b, contains seven identical hexagonal NPs of equal sizes (hexagon side length a) while the NP thicknesses (h) and the interparticle gaps (d) are similar with the quadramer.

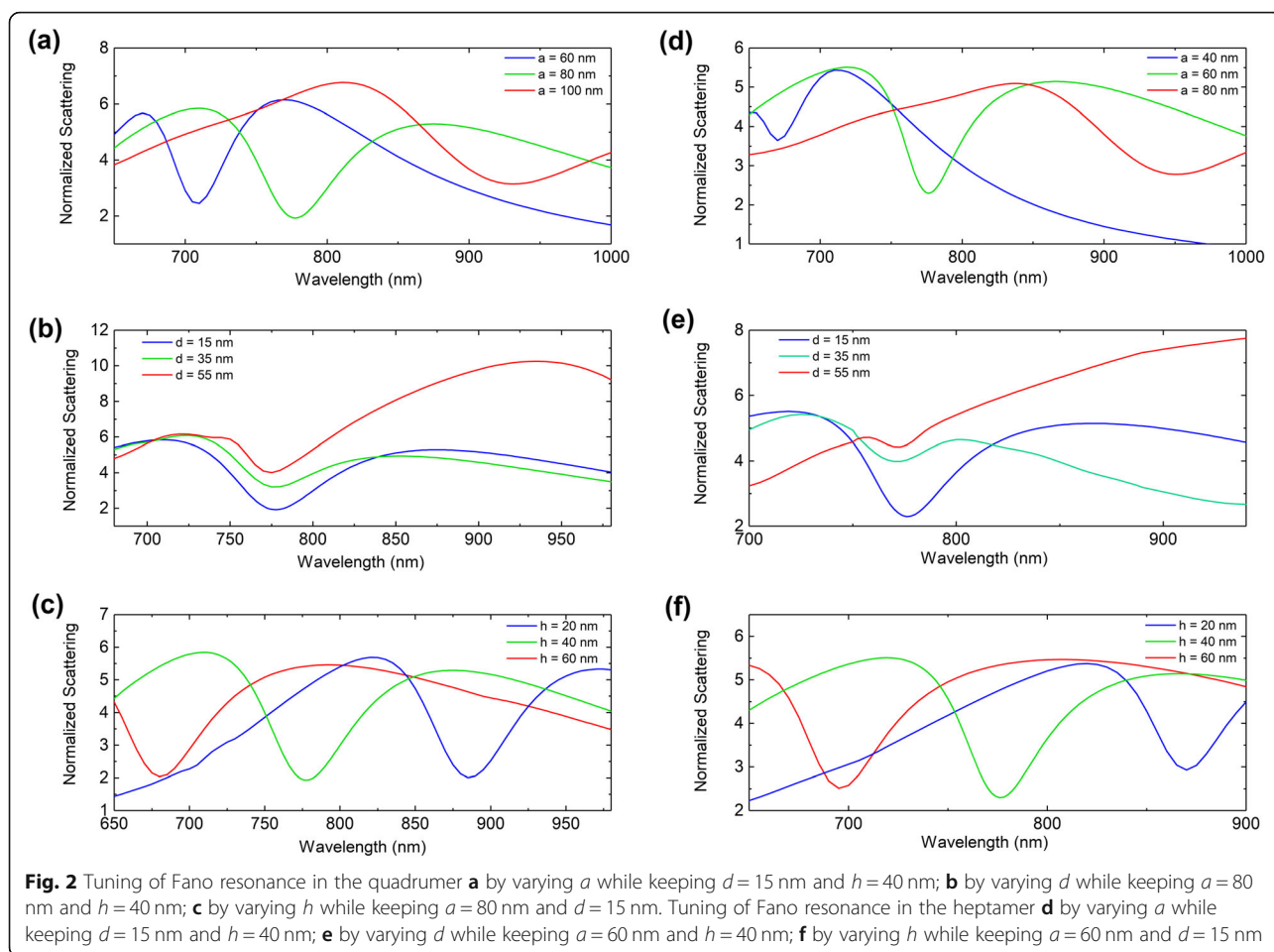
Tuning of FR at the intended spectral regimes was done by optimizing the geometrical parameters of the NPs (i.e. a , d and h). During optimization, effect of one parameter (a , d or h) on FR was studied while keeping all other parameters fixed. An increment in NP size (a) red shifts the Fano dip in both quadramer and heptamer, as depicted in Fig. 2a and d, respectively.

An increment in interparticle gap (d) slightly blue shifts the spectral position of the Fano dip but more importantly reduce the depth of the Fano dip significantly due to the lack of coupling between LSPRs of the NPs, as illustrated in Fig. 2b and e, in the case of the quadramer and the heptamer, respectively. An increment in NP thickness (h) also blue shifts the Fano dip in both quadramer and heptamer, as shown in Fig. 2c and f, respectively. The scattering cross-sections reported in Fig. 2 are normalized by the corresponding geometrical cross-sections.

The scattering profiles of the oligomers were also compared with the so-called Fano-formula [50], mathematically expressed as $\sigma = (\epsilon + q)^2 / (\epsilon^2 + 1)$, where σ is the scattering cross section, q is the asymmetry parameter and ϵ is a parameter related to the reduced energy [50]. Figure 3a depicts a (non-scaled) overlap between the Fano-formula (with $q = 1$) and the scattering lineshape of the oligomers.

As the Fano-formula contains only one maximum and minimum in its lineshape, we quantified the q -parameter in the case of the oligomers as the ratio between the scattering cross-section at the Fano dip (dotted magenta



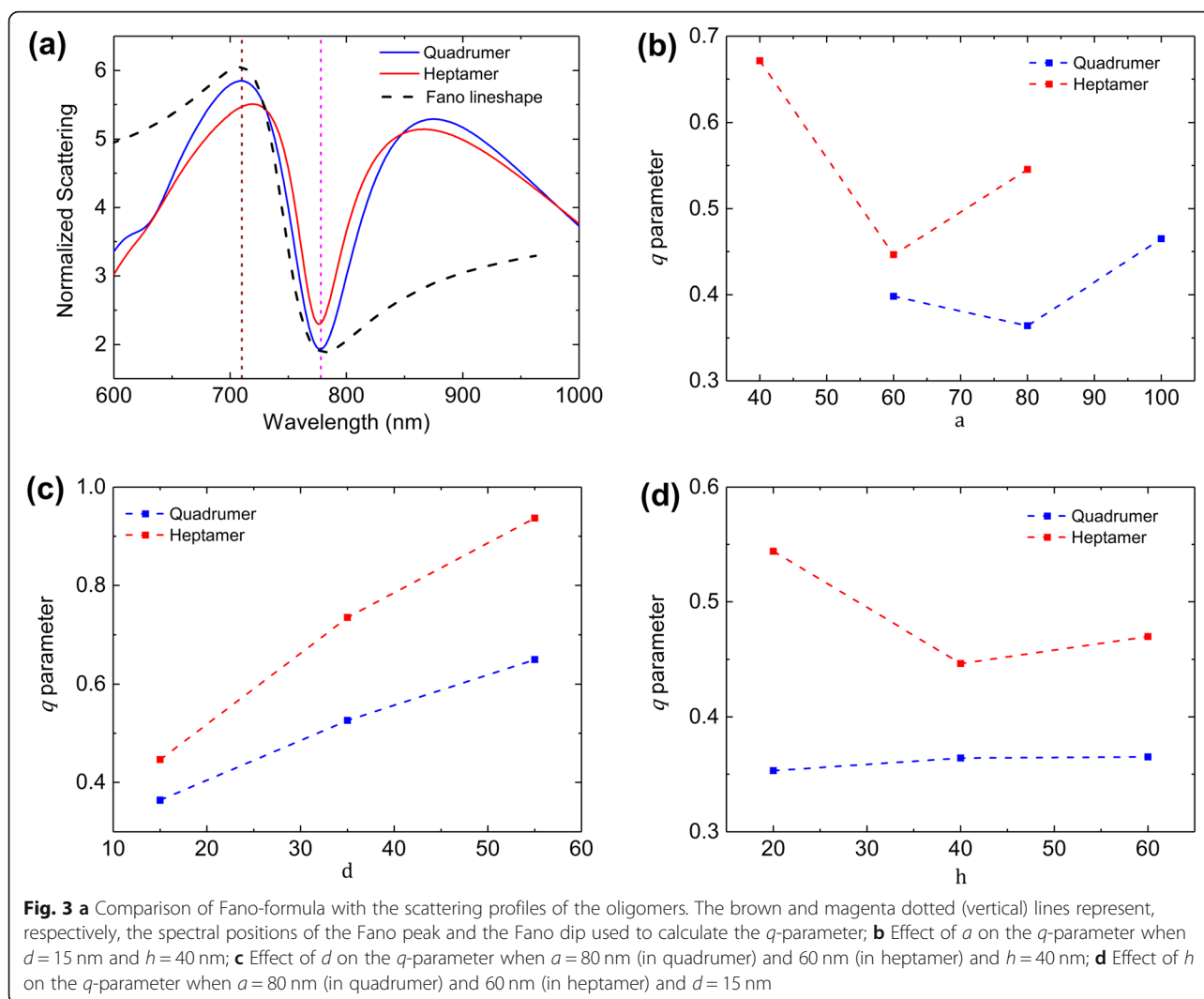


line) and the scattering cross-section at the Fano peak (dotted brown line) in the blue side. Figure 3b, c and d represent the effect of a , d and h on the q -parameter of the oligomers, respectively.

The q -parameter in the case of oligomers not only represents the degree of asymmetry in their corresponding scattering profiles but also quantifies the strength of FR in terms of the depth of the Fano dip (i.e. the strength of the coupling between the LSPR modes of the NPs). Lower the value of q -parameter, higher the depth of the Fano dip, stronger the FR. The strength of FR in a Fano-plasmonic oligomer can directly influence its Raman enhancement capability [45, 51]. Therefore, we optimized the geometrical parameters of the oligomers such a way that their FR spectrally overlapped with the pump, Stokes and CARS regions while maintaining the lowest q -parameter value to ensure the highest Raman enhancement. The optimized geometrical parameters for the quadramer are $a = 80$ nm, $d = 15$ nm and $h = 40$ nm, providing a q -parameter value of 0.36. For the heptamer, the q -parameter value is 0.44 for $a = 62.5$ nm while d and h are similar with the quadramer.

The optimized optical responses of the quadramer and the heptamer are presented in Fig. 4a and b, respectively. In both panels of Fig. 4, the blue curves and the blue vertical axes (on the left side) present the simulated scattering cross-sections of the oligomers (normalized by the corresponding geometrical cross-sections) where the Fano lineshape is profoundly manifested. The Fano dips are clearly in overlap with the pump wavelength (green dashed vertical lines) while the Fano peaks are tune with the Stokes (red shaded rectangular regions) and the CARS (blue shaded rectangular regions) windows for both oligomers.

The red curves and the red vertical axes (on the right side) in both panels of Fig. 4 depict the total near-field intensity enhancement (NFIE) for the oligomers. The NFIE values are calculated as $|E_{loc}/E_0|^2$ integrated over the illuminated surfaces of the hexagonal NPs (i.e. the top and sides walls), where E_{loc} and E_0 are the local and the incident electric field amplitudes, respectively. The NFIE spectra are also normalized by the geometrical surface area of the corresponding illuminated surfaces. From Fig. 4 we can clearly find a spectral correlation between the far-field scattering minima and the NFIE



maxima for both oligomers. In other words, the spectral position of the highest NFIE is very close to the Fano dip in the scattering profile. Such correlation is a general property of Fano-resonant systems, reported earlier in theoretical [52] and experimental studies [45, 51].

The spatial localization of hot spots in such hexagonal NP based oligomers was studied in terms of the near-field enhancement (NFE) maps, computed as $|E_{\text{loc}}/E_0|$ at a plane 1 nm above the top surfaces of the oligomers.

To compare the hot spot localization in hexagon-based oligomers with that of the disk-type oligomers, similar NFE maps were computed for a disk-type quadramer and a disk-type heptamer having similar thicknesses, interparticle gaps and geometrical surface areas corresponds to their hexagonal versions. The NFE maps for the quadramer and the heptamer, calculated at the pump, Stokes and CARS frequencies for the 740 cm^{-1} Raman band of adenine [28], are reported in Figs. 5 and 6, respectively.

To study the localization of hot spots and its effect on SECARS enhancement, we plotted the spatial distribution (or map) of the SECARS (electromagnetic) enhancement factor G in Figs. 5d and 6d for the hexagon-based quadramer and heptamer, respectively. Figures 5h and 6h report the same for the disk-type quadramer and heptamer, respectively. The SECARS electromagnetic enhancement factor is calculated as $G = |E_{\text{loc(pump)}}/E_0|^4 \times |E_{\text{loc(Stokes)}}/E_0|^2 \times |E_{\text{loc(CARS)}}/E_0|^2$ for the 740 cm^{-1} Raman line of adenine [28]. We also assign five hot spot positions in Fig. 5 over the quadramer geometry and six hot spot positions in Fig. 6 over the heptamer geometry, labelled as 'i' to 'vi'.

From Fig. 5 we can clearly see that in the case of hexagon-based quadramer, the hot spots generated at position 'i', 'ii', 'iv', and 'v' spatially overlap at the pump and CARS wavelengths while the hot spot at position 'iii' spatially overlaps at the pump and Stokes wavelengths. Eventually, we achieved all the five hot spots in SECARS

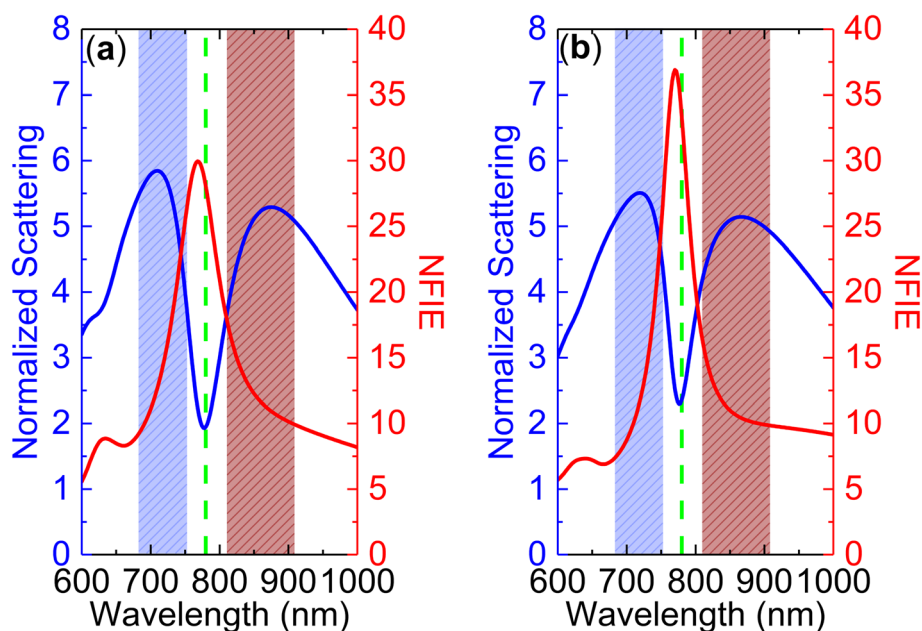


Fig. 4 a Simulated normalized scattering (blue curve) and NFIE (red curve) of the quadrumer; **b** Simulated normalized scattering (blue curve) and NFIE (red curve) of the heptamer. The blue and red vertical axes in both diagrams are corresponded to the blue and red curves present in those diagrams. The green dashed (vertical) lines and the red (blue) shaded rectangular regions in both diagrams depict the pump wavelength (780 nm) and the Stokes (CARS) window for the fingerprint region, respectively

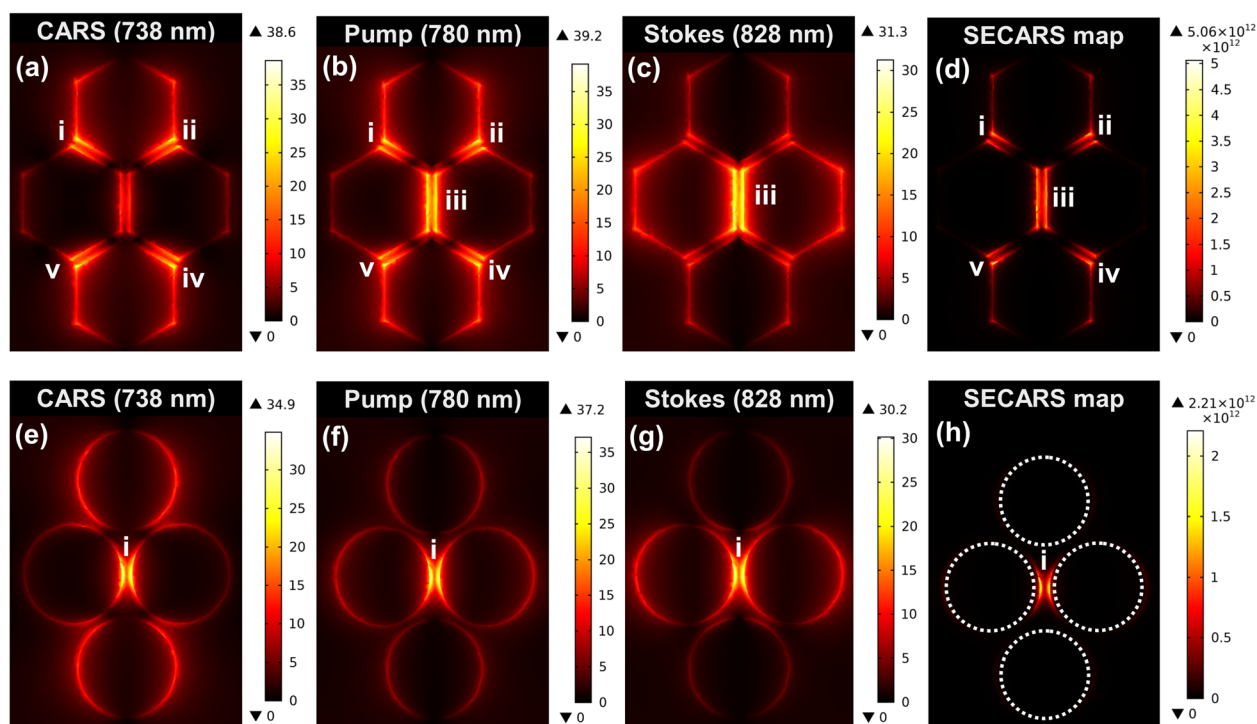
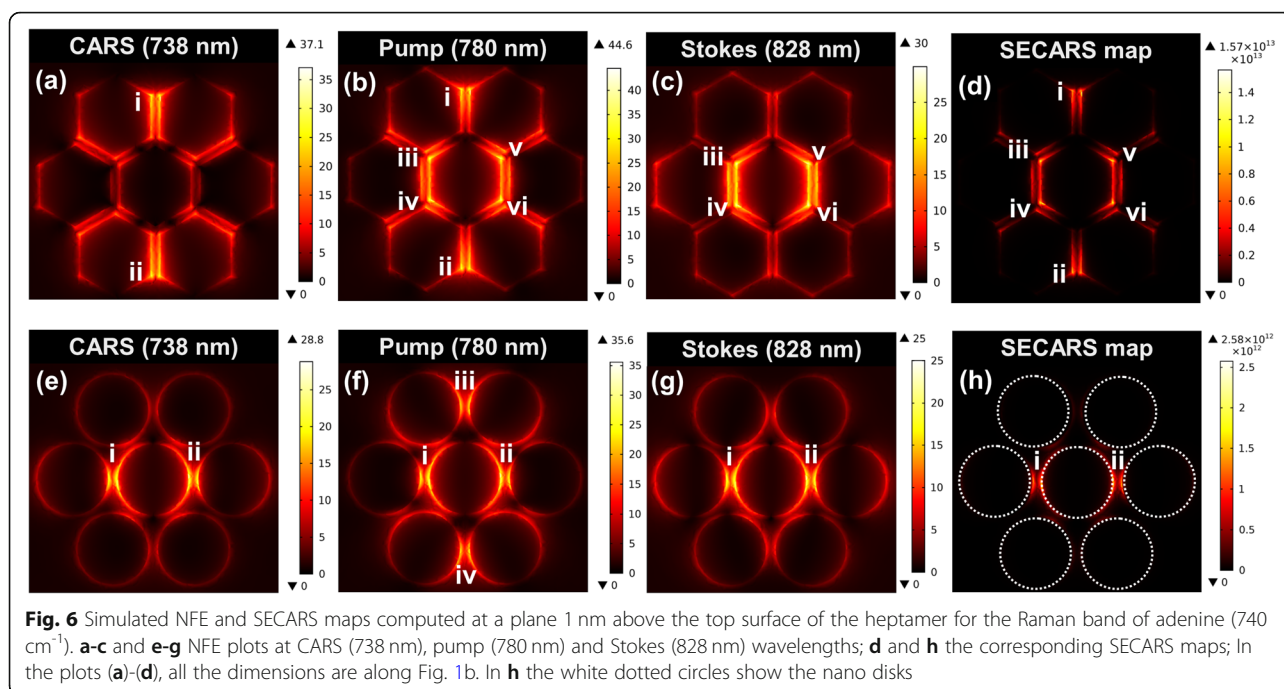


Fig. 5 Simulated NFE and SECARS maps computed at a plane 1 nm above the top surface of the quadrumer for the Raman band of adenine (740 cm^{-1}). **a-c** and **e-g** NFE plots at CARS (738 nm), pump (780 nm) and Stokes (828 nm) wavelengths; **d** and **h** the corresponding SECARS maps; In the plots **(a)-(d)**, all the dimensions are along Fig. 1a. In **h** the white dotted circles show the nano disks



map with an estimated enhancement factor G of 10^{12} at maximum. In the case of disk-type quadrumer, as depicted in Fig. 5e to h, only one hotspot, labelled as 'i', coincides at all three wavelengths and hence, only a single hotspot is obtained in SECARS map with an enhancement factor G of 10^{12} at maximum. For the hexagon-based heptamer, as shown in Fig. 6a to d, the hot spots at positions 'i' and 'ii' spatially overlap at the pump and CARS wavelengths whereas the hot spots at positions 'iii', 'iv', 'v', and 'vi' spatially overlap at the pump and Stokes wavelengths. Consequently, we obtained all the six hot spots in SECARS map with an estimated enhancement factor G of 10^{13} at maximum. However, in the disk-type heptamer, as reported in Fig. 6e to h, the hot spots at positions 'i' and 'ii' spatially overlap at all three wavelengths whereas the hot spots at positions 'iii' and 'iv' are only obtained at the pump wavelength. As a result, only two hotspots, at positions 'i' and 'ii', are obtained in SECARS map with an enhancement factor G of 10^{12} at maximum. The aforementioned findings clearly indicate that we achieved higher number of spatially overlapped hot spots in the hexagon-based oligomers compared to the disk-type oligomers with the normal incidence of excitation light. The predicted enhancement factors (G) for the hexagon-based oligomers are in the order of 10^{12} – 10^{13} , which meet the requirement of single molecular level sensitivity [28]. However, no hot spot is overlapped at all three frequencies (i.e. pump, Stokes and CARS) in the hexagon-based oligomers. Of particular note is that, in the hexagon-based oligomers, the hotspots yielded

higher spatial length compared to the corresponding disk-type versions due to the hexagonal symmetry but without losing the intensity of the field localization.

Achieving higher number of spatially overlapped hot spots with the normal incidence of light is beneficial in the context of hot spot engineering. Generally, hot spots are generated in the oligomers at different spatial locations at different wavelengths and only a few spatially overlapping hot spots at multiple wavelengths can be achieved with the normal incidence of excitation light. Existing literature [30] showed that by applying oblique incidence of excitation light instead of normal incidence, one could increase the number of hot spots over the oligomer geometry because of the spatial redistribution of the localized fields. However, such approach has two limitations. Firstly, the number of hot spots might increase in such approach but in expense of the intensity of the field localization and thereby weakening the total Raman enhancement [30]. Secondly, experimental realization of such approach could become more challenging due to the requirement of precise control on the excitation angle.

Our proposed hexagon-based oligomers provide a way to overcome the aforementioned limitations, by providing higher number of hot spots even with the normal incidence of excitation light and hence, neither losing the intensity of the field localization due to the oblique incidence nor bringing extra constraints in the experimental realization.

The underlying reason behind the generation of FR in those hexagon-based oligomers can be explained in terms of the complex phase relations between the

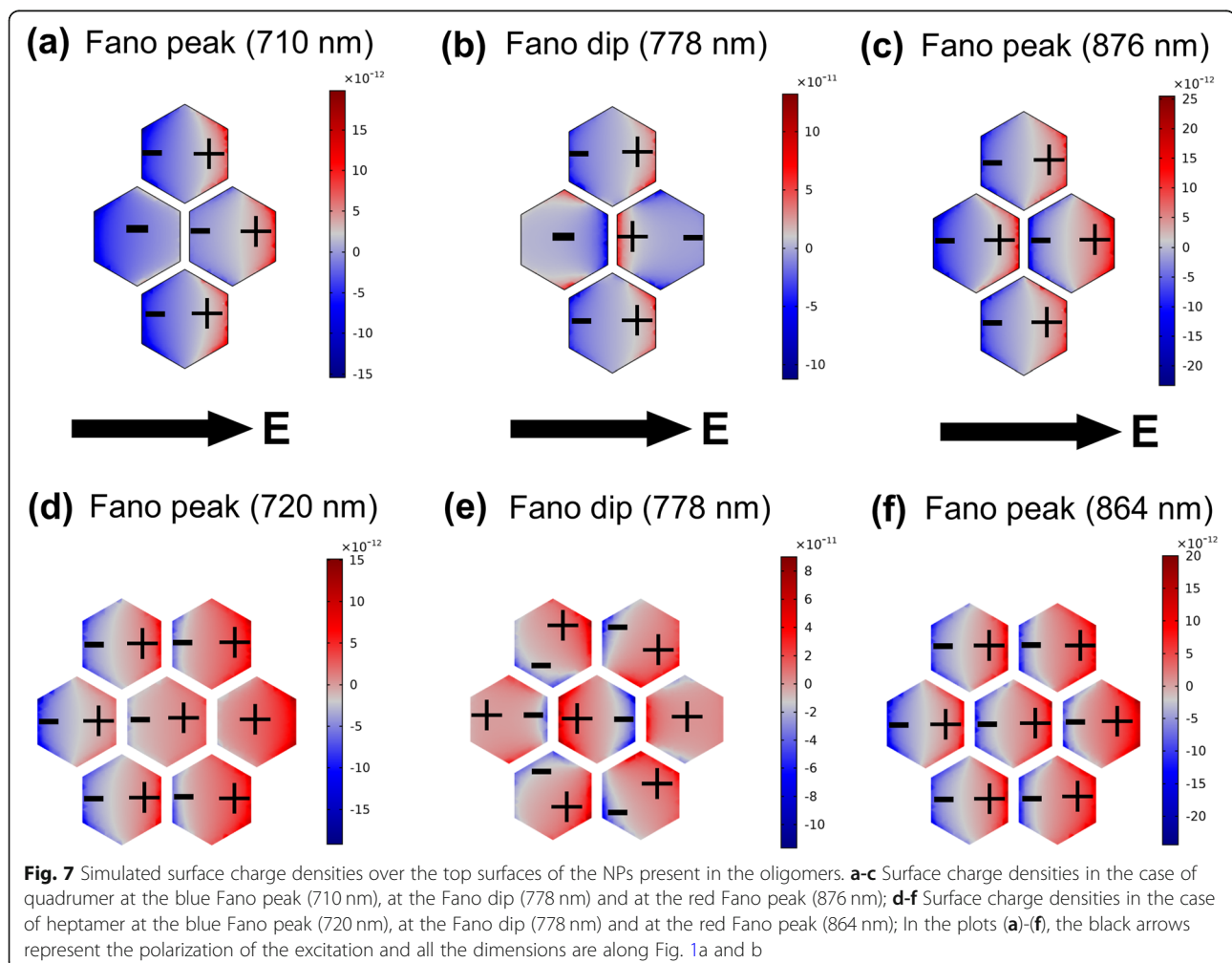
induced dipole moments of the hexagonal NPs. To investigate that, the surface charge densities are calculated over the top surfaces of the NPs present in the hexagon-based oligomers at the Fano peaks and the Fano dips of their corresponding scattering profiles. The surface charge density plots for the hexagon-based quadrumer and heptamer are shown in Fig. 7.

Polarized electromagnetic excitation induces dipole moments on the top surfaces of the NPs present in the oligomers [28, 47]. In the case of hexagon-based quadrumer (Fig. 7a to c), plasmon oscillations (and also the induced dipole moments) in all NPs are ‘in phase’ at the Fano peaks (710 nm and 876 nm) which eventually explains the origin of the broad super-radiant modes of FR as far-field scattering peaks at those wavelengths due to the constructive interference between those dipole moments. At the Fano dip (778 nm), NPs present in the hexagon-based quadrumer maintain an ‘anti-phase’ relation between them. The top and bottom NPs are in phase while the right middle NP is anti-phase with others, as shown in Fig. 7b, and hence, due to the destructive interference between those

dipole moments, a sub-radiant mode is generated at that wavelength in the scattering profile as a dip. In the hexagon-based heptamer (Fig. 7d to f), plasmon oscillations in all NPs are ‘in phase’ at the Fano peaks (720 nm and 864 nm) and like in quadrumer, constructive interference between them explains the generation of the broad super-radiant modes of FR as scattering peaks at the corresponding wavelengths. At the Fano dip (778 nm), NPs in the hexagon-based heptamer manifest a complex phase relation between them, as depicted in Fig. 7e, which is neither ‘anti-phase’ nor ‘in phase’ rather something in between. Consequently, like in quadrumer, the far-field scattering dip or sub-radiant mode of FR is generated due to the destructive interference between the plasmon oscillations in those NPs.

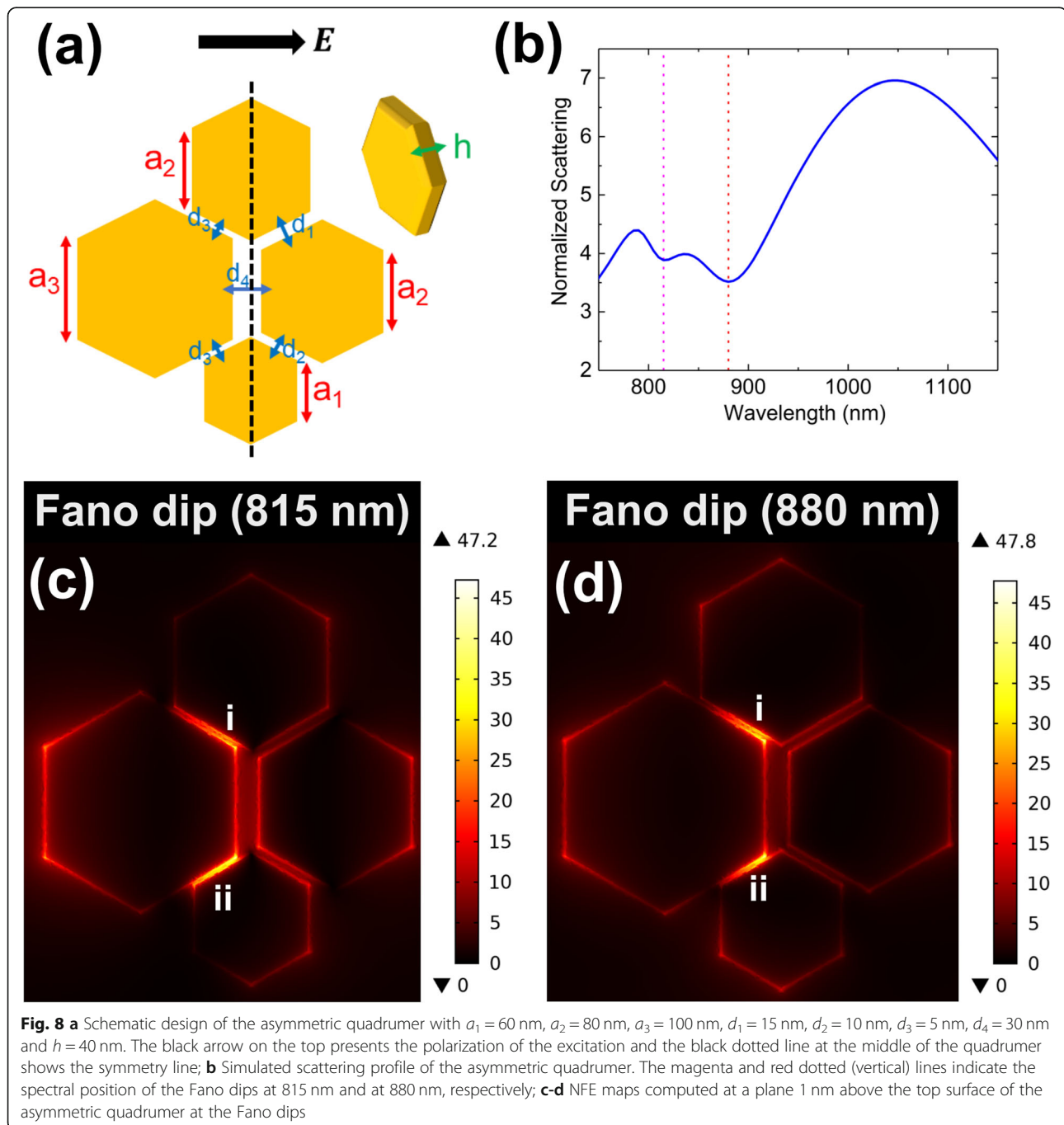
Certainly, we can infer from Fig. 7 that the origin of FR in those hexagon-based oligomers are purely electric in nature since FR originated due to the interaction between the electrical dipole moments of the NPs [28, 40, 46, 47, 53].

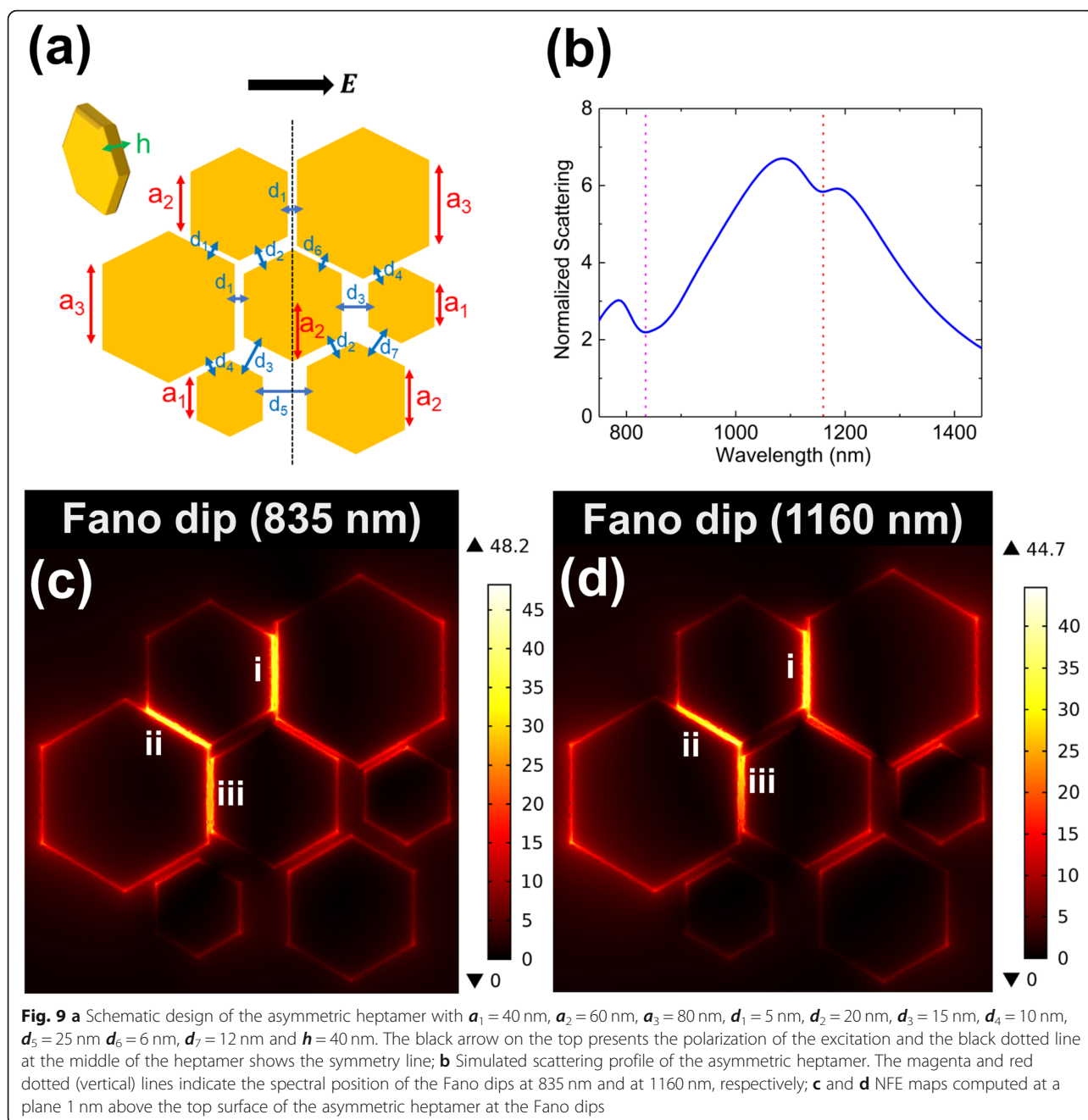
We also investigated the role of the symmetry breaking in the hexagon-based oligomers in terms of the asymmetry



in NP sizes and interparticle gaps with respect to a symmetry line correlated with the polarization of the excitation. Figures 8a and 9a represent the symmetry breaking schematically. In the asymmetric quadrumer, as illustrated in Fig. 8a, the sizes of two NPs were made unequal ($a_1 = 60$ nm, $a_3 = 100$ nm) while keeping the sizes of the rest two NPs equal ($a_2 = 80$ nm). The thicknesses of all four NPs were equal ($h = 40$ nm) but the interparticle gaps were different over the oligomer geometry with $d_1 = 15$ nm, $d_2 = 10$ nm, $d_3 = 5$ nm and $d_4 = 30$ nm. In Fig. 8a, the black

arrow shows the polarization of the excitation light and the black dotted line at the middle of the quadrumer represents the symmetry line. Clearly, the light, polarized along the direction shown in Fig. 8a, will face different NP sizes and interparticle gaps on the two sides of the symmetry line and hence, the symmetry of the oligomer is broken in terms of the polarization of light. Such symmetry breaking in the quadrumer geometry yielded double FR in its scattering profile (Fig. 8b), manifested as two Fano dips at 815 nm (dotted magenta line) and at 880 nm (dotted red line). The





NFE maps at the two Fano dips (Fig. 8c and d) show that we again achieved two hot spots spatially overlapped at both wavelengths.

In the asymmetric heptamer, as illustrated in Fig. 9a, the sizes of four NPs were made unequal ($a_1 = 40$ nm, $a_3 = 80$ nm) while keeping the sizes of the rest three NPs equal ($a_2 = 60$ nm). The thicknesses of all NPs were equal ($h = 40$ nm) but the interparticle gaps were different over the oligomer geometry with $d_1 = 5$ nm, $d_2 = 20$ nm, $d_3 = 15$ nm, $d_4 = 10$ nm, $d_5 = 25$ nm, $d_6 = 6$ nm and $d_7 = 12$ nm. According to Fig. 9a, like in the case of

quadrumer, the light, polarized along the direction shown by the black arrow, will face different NP sizes and interparticle gaps on the two sides of the symmetry line (the black dotted line at the middle of the heptamer) and hence, the symmetry of the oligomer is broken for the polarized light. Here also, profound signature of the double FR was obtained in the scattering profile of the asymmetric heptamer (Fig. 9b) with three hot spots spatially overlapped at both Fano dips (835 nm, dotted magenta line and 1160 nm, dotted red line), as reported in Fig. 9c and d. It is worth to mention here that in the

scattering spectra of asymmetric oligomers (Figs. 8b and 9b), neither any sign of quadrupolar peak was found at the lower wavelengths nor the peaks obtained at higher wavelengths match with the LSPR modes of the individual NPs (i.e. monomer peaks) present in the oligomer. Consequently, we can conclude that the scattering lineshapes are clearly a manifestation of the double FR, generated due to the complex hybridization between the LSPRs of the NPs.

Existence of double FR can also be exploited for SECARS enhancements by tuning the two Fano dips at the pump and Stokes wavelengths while the Fano peak (at the blue side of the both Fano dips) at the CARS wavelength. Such strategy will ensure minimization of scattering losses and efficient energy coupling between the oligomer and the excitation light at both excitation wavelengths (i.e. pump and Stokes) as well as an enhanced far-field propagation of CARS signal [30].

Generation of double FR in the optical responses of those hexagon-based oligomers is not a general effect of symmetry breaking and since, symmetry can be broken in different possible ways, it can also affect the optical response of the oligomers differently. Further studies required to draw any concrete conclusion on the role of symmetry breaking in such hexagon-based oligomers.

Conclusions

Succinctly, we designed hexagonal NP based Fano-resonant oligomers, a gold quadrumer and a gold heptamer, using FEM simulations for optimal performance in CARS applications at 780 nm pumping. The targeted Raman signature zone was the 'fingerprint region' ($500\text{--}1800\text{ cm}^{-1}$) of the analytes. Our proposed designs provide fabrication possible geometries for the oligomers. We achieved to engineer the lineshape of the FR in those oligomers so that the sub-radiant mode of FR would spectrally overlap with the pump to ensure energy coupling between the excitation light and the nanostructures while the super-radiant modes of FR would tune with the Stokes and CARS regimes to enhance far-field propagation of the output light. Our computational studies revealed that the hexagonal NP based oligomers yielded higher number of spatially overlapped hot spots compared to the disk-type oligomers even in the case of normal incidence of excitation light. Our estimated SECARS enhancements from the proposed oligomers were in the order of $10^{12}\text{--}10^{13}$, which meet the requirement of single molecular level applications. We also explored the origin of the FR in those oligomers, which is purely electric in nature. Our studies on the role of symmetry breaking in the proposed oligomers provided a way to implement double FR in such structures and enabled its exploitation for SECARS by yielding spatially overlapped hot spots at multiple Fano dips. Such

numerical findings are important in the context of designing plasmonic substrates with fabrication-friendly nanostructures for SECARS and for multi-photon based spectroscopic techniques in general to realize higher number of spatially localized hotspots for improving the detection sensitivity.

Abbreviations

CARS: Coherent anti-Stokes Raman scattering; FEM: Finite element method; FR: Fano resonance; FWM: Four-wave mixing; LSPR: Localized surface plasmon resonances; NFE: Near-field enhancement; NFIE: Near-field intensity enhancement; NPs: Nanoparticles; PMLs: Perfectly matched layers; RS: Raman spectroscopy; SECARS: Surface-enhanced coherent anti-Stokes Raman scattering; SERS: Surface-enhanced Raman spectroscopy

Acknowledgements

The authors gratefully acknowledge Prof. Kai-Erik Peiponen (University of Eastern Finland), Prof. Mika Pettersson (University of Jyväskylä), and Assoc. Prof. J. Jussi Toppari (University of Jyväskylä) for their valuable guidance during the research work.

Authors' contributions

A. Dutta proposed the original idea and implemented the simulations. E. M. Vartiainen guided the research. A. Dutta drafted and wrote the manuscript. Both authors read, revised and approved the final manuscript.

Funding

The work is part of the Academy of Finland Flagship Program, Photonics Research and Innovation (PREIN), decision 321066.

Availability of data and materials

Information about data was detailed in the article.

Ethics approval and consent to participate

Not applicable.

Consent for publication

Not applicable.

Competing interests

The authors declare that they have no competing interests.

Author details

¹Department of Physics and Nanoscience Center, University of Jyväskylä, Jyväskylä, Finland. ²School of Engineering Science, LUT University, Lappeenranta, Finland.

Received: 1 December 2019 Accepted: 24 February 2020

Published online: 09 April 2020

References

1. Long, D.: Early history of the Raman effect. *Int. Rev. Phys. Chem.* **7**(4), 317–349 (1988)
2. Banwell, C.: Raman spectroscopy. In: Banwell, C. (ed.) *Fundamentals of Molecular Spectroscopy*, pp. 124–154. McGraw-Hill, New York (1972)
3. Long, D.: *The Raman Effect: a Unified Treatment of the Theory of Raman Scattering by Molecules*. Wiley, New Jersey (2002)
4. Shipp, D., Sinjab, F., Nottingher, I.: Raman spectroscopy: techniques and applications in the life sciences. *Adv. Opt. Photonics.* **9**(2), 315–428 (2017)
5. Das, R., Agrawal, Y.: Raman spectroscopy: recent advancements, techniques and applications. *Vib. Spectrosc.* **57**, 163–176 (2011)
6. Vandenabeele, P., Tate, J., Moens, L.: Non-destructive analysis of museum objects by fiber-optic Raman spectroscopy. *Anal. Bioanal. Chem.* **387**(3), 813–819 (2007)
7. Meksiarun, P., Andriana, B., Matsuyoshi, H., Sato, H.: Non-invasive quantitative analysis of specific fat accumulation in subcutaneous adipose tissues using Raman spectroscopy. *Sci. Rep.* **6**, 37068 (2016)
8. Haynes, C., McFarland, A., Van Duyne, R.: Surface-enhanced Raman spectroscopy. *Anal. Chem.* **77**(17), 338A–346A (2005)

9. Schlücker, S.: Surface-enhanced Raman spectroscopy: concepts and chemical applications. *Angew. Chem. Int. Ed.* **53**, 4756–4795 (2014)
10. Sharma, B., Frontiera, R., Henry, A., Ringe, E., Van Duyne, R.: SERS: materials, applications, and the future. *Mater. Today*. **15**(1–2), 16–25 (2012)
11. Ding, S., You, E., Tian, Z., Moskovits, M.: Electromagnetic theories of surface-enhanced Raman spectroscopy. *Chem. Soc. Rev.* **46**, 4042–4076 (2017)
12. Chulhai, D., Hu, Z., Moore, J., Chen, X., Jensen, L.: Theory of linear and nonlinear surface-enhanced vibrational spectroscopies. *Annu. Rev. Phys. Chem.* **67**, 541–564 (2016)
13. Henry, A., Sharma, B., Cardinal, M., Kurouski, D., Van Duyne, R.: Surface-enhanced Raman spectroscopy biosensing: in vivo diagnostics and multimodal imaging. *Anal. Chem.* **88**, 6638–6647 (2016)
14. Tripp, R., Dluhy, R., Zhao, Y.: Novel nanostructures for SERS biosensing. *Nano Today*. **3**(3–4), 31–37 (2008)
15. Bantz, K., Meyer, A., Wittenberg, N., Im, H., Kurtulus, Ö., Lee, S., Lindquist, N., Oh, S.H., Haynes, C.: Recent progress in SERS biosensing. *Phys. Chem. Chem. Phys.* **13**, 11551–11567 (2011)
16. Ru, E., Etchegoin, P.: Single-molecule surface-enhanced Raman spectroscopy. *Annu. Rev. Phys. Chem.* **63**, 65–87 (2012)
17. Wang, Y., Irudayaraj, J.: Surface-enhanced Raman spectroscopy at single-molecule scale and its implications in biology. *Phil. Trans. R Soc. B.* **368**, 20120026 (2013)
18. Lee, H., Jin, S., Kim, H., Suh, Y.: Single-molecule surface-enhanced Raman spectroscopy: a perspective on the current status. *Phys. Chem. Chem. Phys.* **15**, 5276–5287 (2013)
19. Zrimsek, A., Chiang, N., Mattei, M., Zaleski, S., McAnally, M., Chapman, C., Henry, A.I., Schatz, G., Van Duyne, R.: Single-molecule chemistry with surface- and tip-enhanced Raman spectroscopy. *Chem. Rev.* **117**, 7583–7613 (2017)
20. Eesley, G.: *Coherent Raman Spectroscopy*. Pergamon Press, Oxford (1981)
21. Cheng, J.X., Xie, X.S. (eds.): *Coherent Raman Scattering Microscopy*. CRC Press, Boca Raton (2013)
22. Evans, C.L., Xie, X.S.: Coherent anti-Stokes Raman scattering microscopy: chemical imaging for biology and medicine. *Annu. Rev. Anal. Chem.* **1**, 883–909 (2008)
23. Cheng, J.X., Xie, X.S.: Coherent anti-Stokes Raman scattering microscopy: instrumentation, theory, and applications. *J. Phys. Chem. B.* **108**(3), 827–840 (2004)
24. Volkmer, A.: Vibrational imaging and microspectroscopies based on coherent anti-Stokes Raman scattering microscopy. *J. Phys. D: Appl. Phys.* **38**, R59–R81 (2005)
25. Krafft, C., Dietzek, B., Schmitt, M., Popp, J.: Raman and coherent anti-Stokes Raman scattering microspectroscopy for biomedical applications. *J. Biomed. Opt.* **17**(4), 0408011–04080115 (2012)
26. Volkmer, A.: Coherent Raman scattering microscopy. In: Matousek, P., Morris, M. (eds.) *Emerging Raman Applications and Techniques in Biomedical and Pharmaceutical Fields*, pp. 111–152. Springer – Verlag, Berlin (2010)
27. Xie, X.S., Cheng, J., Potma, E.: Coherent anti-Stokes Raman scattering microscopy. In: Pawley, J.B. (ed.) *Handbook of Biological Confocal Microscopy*, pp. 595–606. Springer – Verlag US, Boston (2006)
28. Zhang, Y., Zhen, Y., Neumann, O., Day, J., Nordlander, P., Halas, N.: Coherent anti-Stokes Raman scattering with single-molecule sensitivity using a plasmonic Fano resonance. *Nat. Commun.* **5**, 4424 (2014)
29. Zhou, Q., Zhu, J., Yuan, J., Fang, X.: Numerical simulation of surface-enhanced coherent anti-Stokes Raman scattering on gold nanoparticle substrate. *J. Nanosci. Nanotechnol.* **17**(3), 2152–2156 (2017)
30. He, J., Fan, C., Ding, P., Zhu, S., Liang, E.: Near-field engineering of Fano resonances in a plasmonic assembly for maximizing CARS enhancements. *Sci. Rep.* **6**, 20777 (2016)
31. Hentschel, M., Dregely, D., Vogelgesang, R., Giessen, H., Liu, N.: Plasmonic oligomers: the role of individual particles in collective behavior. *ACS Nano*. **5**(3), 2042–2050 (2011)
32. Hentschel, M., Saliba, M., Vogelgesang, R., Giessen, H., Alivisatos, P., Liu, N.: Transition from isolated to collective modes in plasmonic oligomers. *Nano Lett.* **10**(7), 2721–2726 (2010)
33. Zhang, Y., Wen, F., Zhen, Y.R., Nordlander, P., Halas, N.: Coherent Fano resonances in a plasmonic nanocluster enhance optical four-wave mixing. *Proc. Natl. Acad. Sci. U. S. A.* **110**(23), 9215–9219 (2013)
34. Fan, J., Bao, K., Wu, C., Bao, J., Bardhan, R., Halas, N., Manoharan, V., Shvets, G., Nordlander, P., Capasso, F.: Fano-like interference in self-assembled plasmonic quadrumer clusters. *Nano Lett.* **10**(11), 4680–4685 (2010)
35. Gallinet, B., Martin, O.: Influence of electromagnetic interactions on the line shape of plasmonic Fano resonances. *ACS Nano*. **5**(11), 8999–9008 (2011)
36. Lassiter, B., Sobhani, H., Knight, M., Mielczarek, W., Nordlander, P., Halas, N.: Designing and deconstructing the Fano lineshape in plasmonic nanoclusters. *Nano Lett.* **12**, 1058–1062 (2012)
37. Lassiter, B., Sobhani, H., Fan, J., Kundu, J., Capasso, F., Nordlander, P., Halas, N.: Fano resonances in plasmonic nanoclusters: geometrical and chemical tenability. *Nano Lett.* **10**(8), 3184–3189 (2010)
38. Joe, Y., Satanin, A., Kim, C.: Classical analogy of Fano resonances. *Phys. Scr.* **74**, 259–266 (2006)
39. Lovera, A., Gallinet, B., Nordlander, P., Martin, O.: Mechanisms of Fano resonances in coupled plasmonic systems. *ACS Nano*. **7**(5), 4527–4536 (2013)
40. Rahmani, M., Tahmasebi, T., Lin, Y., Lukiyanchuk, B., Liew, T., Hong, M.: Influence of plasmon destructive interferences on optical properties of gold planar quadrumers. *Nanotechnology*. **22**, 245204 (2011)
41. Rahmani, M., Lei, D., Giannini, V., Lukiyanchuk, B., Ranjbar, M., Liew, T., Hong, M., Maier, S.: Subgroup decomposition of plasmonic resonances in hybrid oligomers: modeling the resonance lineshape. *Nano Lett.* **12**(4), 2101–2106 (2012)
42. Attaran, A., Emami, S., Soltanian, M., Penny, R., Behbahani, F., Harun, S., Ahmad, H., Abdul-Rashid, H., Moghavvemi, M.: Circuit model of Fano resonance on tetramers, pentamers and broken symmetry pentamers. *Plasmonics*. **9**, 1303–1313 (2014)
43. Gallinet, B., Martin, O.: Ab-initio theory of Fano resonances in plasmonic nanostructures and metamaterials. *Phys. Rev. B.* **83**, 2354271–2354276 (2011)
44. Hashimoto, K., Omachi, J., Ideguchi, T.: Ultra-broadband rapid-scan Fourier-transform CARS spectroscopy with sub-10-fs optical pulses. *Opt. Express*. **26**, 14307–14314 (2018)
45. Ye, J., Wen, F., Sobhani, H., Lassiter, J., Dorpe, P., Nordlander, P., Halas, N.: Plasmonic nanoclusters: near-field properties of the Fano resonance interrogated with SERS. *Nano Lett.* **12**(3), 1660–1667 (2012)
46. Rahmani, M., Lukiyanchuk, B., Ng, B., Tavakkoli, A., Liew, T., Hong, M.: Generation of pronounced Fano resonances and tuning of subwavelength spatial light distribution in plasmonic pentamers. *Opt. Express*. **19**(6), 4949–4956 (2011)
47. Rahmani, M., Lukiyanchuk, B., Nguyen, T., Tahmasebi, T., Lin, Y., Liew, T., Hong, M.: Influence of symmetry breaking in pentamers on Fano resonance and near-field energy localization. *Opt. Mater. Express*. **1**(8), 1409–1415 (2011)
48. COMSOL Multiphysics v. 5.4. Application: Scatterer on Substrate. COMSOL AB, Stockholm. https://www.comsol.fi/model/download/563151/models.woptics.scatterer_on_substrate.pdf. Accessed 1 Dec 2019 (2019)
49. Johnson, P., Christy, R.: Optical constants of the noble metals. *Phys. Rev. B.* **6**, 4370–4379 (1972)
50. Miroshnichenko, A., Flach, S., Kivshar, Y.: Fano resonances in nanoscale structures. *Rev. Mod. Phys.* **82**, 2257–2298 (2010)
51. Dutta, A., Alam, K., Nuutinen, T., Hultko, E., Karvinen, P., Kuittinen, M., Toppari, J.J., Vartiainen, E.: Influence of Fano resonance on SERS enhancement in Fano-plasmonic oligomers. *Opt. Express*. **27**(21), 30031–30043 (2019)
52. Gallinet, B., Martin, O.: Relation between near-field and far-field properties of plasmonic Fano resonances. *Opt. Express*. **19**(22), 22167–22175 (2011)
53. Rahmani, M., Lukiyanchuk, B., Tahmasebi, T., Lin, Y., Liew, T., Hong, M.: Polarization-controlled spatial localization of near-field energy in planar symmetric coupled oligomers. *Appl. Phys. A Mater. Sci. Process.* **107**, 23–30 (2012)

Publisher's Note

Springer Nature remains neutral with regard to jurisdictional claims in published maps and institutional affiliations.